

Low-order network modeling of an industrial thermoacoustic rig using Bayesian data assimilation

Symposium on Thermoacoustics in
Combustion: Industry meets Academia
(SoTIC 2025)
Sept. 8 - Sept. 11, 2025
Trondheim, Norway
Paper No.: 14
©The Author(s) 2025

Jingquan Zheng¹ Matthew Yoko¹ André Fischer² Claus Lahiri² and Matthew Juniper¹

Abstract

Accurate and computationally efficient modeling of thermoacoustic instabilities would help effective development of low-emission combustion technologies. In this paper, we develop a low-order network model (LONM) for non-reacting and reacting flows in the SCARLET (SCaled Acoustic Rig for Low Emission Technologies) test rig and optimize model parameters in the reacting case with Bayesian inference into physical models. For the non-reacting flow, a combination of area jump and duct network elements models the complex injector, which has several axial swirlers. We model these swirlers as duct elements with effective areas derived from experiments. The network predicts the non-reacting mean flow field and acoustic field with less than 2 % and 10 % discrepancy with respect to the experimental measurements across different operating conditions. For the reacting case, we model the flame as a compact flame and derive an injector-geometry-based flame transfer function (FTF). The initial reacting model showed significant acoustic discrepancy due to the uncertain parameters within the FTF. We then assimilate experimental data to optimize the uncertain parameters of the FTF by minimizing the negative log-posterior likelihood of the parameters, given the prior assumptions and the data. After data assimilation, the network predicts the reacting mean flow field and acoustic field with a discrepancy less than 1 % and 24 %, respectively. This assimilation process reduces the acoustic model error by 38 % compared to the reacting model without assimilation. This paper shows that the LONM can accurately predict the mean flow field and acoustic response of the SCARLET rig. Furthermore, Bayesian data assimilation significantly improves the reacting model's predictive accuracy and shows the most influential parameters of the model, which enhances physical insights into the flame response with respect to the acoustic perturbation.

Keywords

Thermoacoustic, Low-order Network, Injector Modeling, Flame Transfer Function, Bayesian Inference

Introduction

Thermoacoustic oscillations are key problems in the design of advanced rockets and gas turbines (Culick 2006; Poinso 2017). The accurate prediction and passive control of oscillations have remained elusive for decades due to their inherent and extreme sensitivity to model accuracy (Juniper and Sujith 2018).

The modeling of thermoacoustic instabilities typically relies on two main strategies: high-fidelity computational fluid dynamics (CFD) and computationally efficient reduced-order models (ROMs). While CFD approaches (Cannon et al. 2001; Poinso 2017) provide detailed physical insights into the intricate coupling between acoustics, flow, and flame dynamics, their substantial computational expense often renders them impractical for rapid iteration during the early stages of industrial design. In contrast, the low-order network method (Dowling and Stow 2003), a type of ROM, simplifies system geometries and complex flame behaviours into a series of interconnected acoustic elements and jump conditions. This approach is fast, efficient, and qualitatively accurate, making it valuable for preliminary industrial design. However, a limitation of these network models is their lack of quantitative precision, particularly in modelling the flame response to acoustic perturbations, which is usually described by the FTF (Hubbard and Dowling 2001).

Methodologies for determining FTFs fall into three categories: extraction from experimental measurements (Eder et al. 2024), CFD simulations (Han and Morgans 2015), or development via analytical modeling (Crocco 1951; Schuermans et al. 2004; Polifke and Lawn 2007). The extraction of FTFs from experimental data or CFD simulations is expensive. A further limitation is that such FTFs, defined at discrete forcing frequencies, cannot always be safely interpolated to unmeasured frequencies or reliably extrapolated beyond the investigated range. In contrast, the analytical methods mitigate this constraint. Analytical methods also show how different parameters (e.g., the bulk mean velocity, pressure, equivalence ratio) influence the flame response. However, they often involve significant simplifications and may not capture the full complexity of real flame dynamics. Their model accuracy is limited, especially outside the range

¹ University of Cambridge, Department of Engineering, UK

² Rolls-Royce Deutschland, Dahlewitz, DE

Corresponding author:

Matthew Juniper
Department of Engineering
Cambridge, CB21PZ, United Kingdom

Email: mpj1001@cam.ac.uk

of the underlying assumptions (Crocco 1951). These limitations can be mitigated with physics-based Bayesian inference data assimilation Juniper and Yoko (2022); Yoko and Juniper (2024).

In this paper, we focus on developing and assimilating data into a low-order network model for both non-reacting and reacting flows within the SCARLET rig (Fischer and Lahiri 2021; Çetin Ozan Alanyalıoğlu et al. 2024). We develop an injector-geometry-based FTF and apply physics-based Bayesian inference to assimilate experimental data. This approach optimizes the uncertain FTF parameters, thereby significantly improving the model accuracy for the reacting flow based on this data. This work demonstrates that the development of an LONM is capable of accurately modelling the mean flow field and acoustic response in a complex industrial rig. Furthermore, it highlights how Bayesian data assimilation can substantially refine the model's accuracy for the reacting condition, offering a pathway to more reliable and quantitatively accurate low-order modeling for thermoacoustic instabilities in advanced combustion technologies.

Methodology

Experiments

The Rolls-Royce SCARLET thermoacoustic test rig is an industrial-scale combustion test facility to investigate the acoustic and flame response of different fuel injectors under realistic operating conditions. As shown in Fig. 1, the experimental facility includes measurement sections upstream and downstream of the combustor, a combustion module equipped with an easily exchangeable fuel spray nozzle, four acoustic excitation sirens, and a backpressure valve. The sirens generate sinusoidal acoustic excitation of a defined amplitude over the frequency range from 100 Hz to 1200 Hz (Fischer and Lahiri 2021). For each frequency, the rig is sequentially forced first from the upstream and then downstream end. There are 10 microphones to measure the acoustic pressure upstream and downstream of the test section. Acoustic dampers located at the inlet and outlet provide well-defined boundary conditions by minimizing reflections and preventing acoustic resonances within the rig. The combustor geometry, featuring an effusion-cooled liner, conceptually resembles that of an aero-engine combustor.

Fig. 2 shows that the test section is a combustion chamber, in which the incoming flow splits into the injector, heatshield and outer annulus through the metering plate. The injector itself is a dual-circuit (main and pilot) design employing axial swirl stabilization and prefilming air-blast atomizer for Jet-A1 fuel.

In this study, as shown in Table 1, we focus on three non-reacting experiments (NR1, NR2 and NR3) and one reacting experiment (R1). The R1 case supplies fuel only to the main injector to isolate the flame characteristics of the main flame. We vary the inlet pressure, temperature, and mass flow rate across the non-reacting cases in order to assess the predictive performance of our network model under different operating conditions.

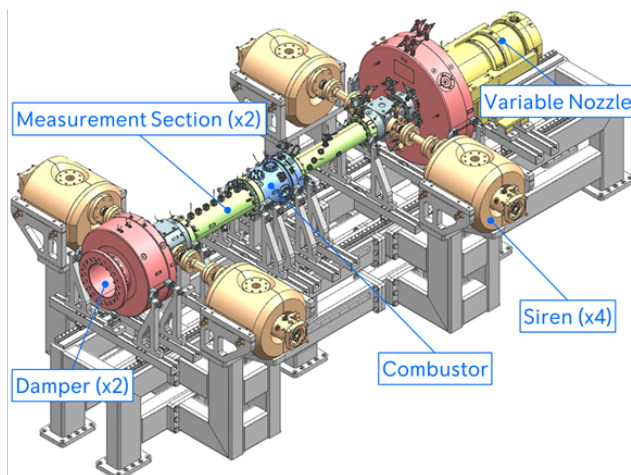


Figure 1. An isometric view of the SCARLET rig. The flow comes from left to right.

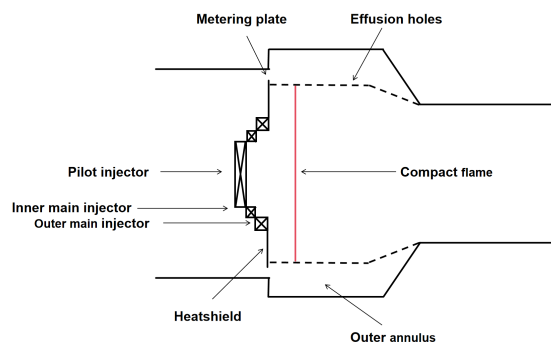


Figure 2. A schematic of the test section (combustor) of the SCARLET rig (not to scale)

Table 1. Reacting and non-reacting experimental conditions.

Case	Inlet Pressure (MPa)	Inlet Temp. (K)	Air Mass Flow (kg/s)
NR1	1.88	775	2.79
NR2	1.53	728	2.37
NR3	2.95	827	3.93
R1	2.91	839	4.06

Low order network for the non-reacting and reacting SCARLET rig

Injector modelling In the injector section of Fig. 2, the flow splits into the outer main, inner main and pilot circuits. The flows from the outer main and inner main circuits combine to feed the main nozzle. In each flow passage, there is a corresponding axial swirler. In this study, we only consider the axial acoustic mode and we model these swirlers as a combination of area increase, straight duct and area decrease network elements. The effective area of the straight duct for each swirler is extracted from the pressure drop across the injector and from LES (Reinhardt et al. 2023). The three network elements are described in Zheng et al. (2024); Aguilar et al. (2017). The network models for the ‘path-split’ and ‘join-in’ are described below.

A path split model has one inlet duct that connects to multiple outlet ducts. Similar to the area decrease

element (Dowling and Stow 2003), the governing equations are the conservation of mass, and the isentropic and isenthalpic conditions:

$$m_i = \sum_{j=1}^N m_{o,j} \quad (1)$$

$$s_i = s_{o,j} \quad \text{for } j = 1, 2, \dots, N \quad (2)$$

$$h_i = h_{o,j} \quad \text{for } j = 1, 2, \dots, N \quad (3)$$

A path join-in model has multiple inlet ducts that join into one outlet duct. The governing equations are the conservation of mass, momentum, energy and the pressure matching condition:

$$\sum_{j=1}^N m_{i,j} = m_o \quad (4)$$

$$\sum_{j=1}^N M_{i,j} = M_o \quad (5)$$

$$\sum_{j=1}^N E_{i,j} = E_o \quad (6)$$

$$p_{i,1} = p_{i,2} = \dots = p_{i,N} \quad (7)$$

Injector-geometry-based flame transfer function As shown in Fig. 2, we model the swirling main flame as a compact flame element. The governing equations across this element are the conservation of mass Eq. (4), momentum Eq. (5), and energy equations:

$$E_i + \dot{Q} = E_o \quad (8)$$

The heat release rate \dot{Q} can be defined as Schuermans et al. (2004):

$$\dot{Q} = \rho_i S_f A_f y_i h_f \quad (9)$$

where S_f is the turbulent burning velocity, A_f is the flame surface area, $y_i = \frac{m_f}{m_f + m_a}$ is the mixture fraction and h_f is the specific chemical enthalpy of the fuel. We linearize Eq. (9) and obtain perturbations of the reacting flow, leading to fluctuations of the heat release rate.

$$\frac{\delta \dot{Q}}{\dot{Q}} = \frac{\delta \rho_i}{\rho_i} + \frac{\delta A_f}{A_f} + \frac{\delta S_f}{S_f} + \frac{\delta y_i}{y_i} \quad (10)$$

We ignore the density perturbation and assume that the injector is stiff, meaning that the perturbation of the fuel supply is negligible (Polifke and Lawn 2007). The mixture fraction perturbation before the flame δy_i is therefore proportional to the equivalence ratio perturbation $\delta \phi_i$ and

inversely proportional to the velocity perturbation δu_i .

$$\delta y_i(t) \propto \delta \phi_i(t) \propto \delta u_i^{-1}(t) \quad (11)$$

In the main flame only case, the velocity perturbation $\delta u_i(t)$ in Eq. (11) originates from induced vorticity waves in the outer and inner main swirlers. These waves are convected downstream to the flame front. Based on Eq. (4) and ignoring the density variation, we obtain:

$$\begin{aligned} \frac{\delta y_i(t)}{y_i} &= -\frac{\delta u_i(t)}{u_i} \\ &= -\frac{A_{om} \delta u_{om}(t - \tau_{om}) + A_{im} \delta u_{im}(t - \tau_{im})}{A_i u_i} \end{aligned} \quad (12)$$

where A_{om} and A_{im} are the respective cross-sectional areas downstream of the outer and inner main swirlers, and δu_{om} and δu_{im} are the swirler-induced velocity perturbations. The associated time delays for convection of these perturbations to the compact flame position are τ_{om} and τ_{im} .

The turbulent burning velocity S_f depends on the velocity u_i and equivalence ratio ϕ_i before the flame front, where the exponents x and y in Eq. (13) define the dependence of S_f on u_i and ϕ_i , respectively.

$$S_f(t) \propto u_i^x(t) \phi_i^y(t) \propto u_i^{x-y}(t) \quad (13)$$

Based on Eq. (13), we obtain a relationship between $\frac{\delta S_f(t)}{S_f}$ and $\frac{\delta u_i(t)}{u_i}$:

$$\frac{\delta S_f(t)}{S_f} = (x - y) \frac{\delta u_i(t)}{u_i} \quad (14)$$

The flame surface area A_f is proportional to u_i and inversely proportional to S_f at the flame front.

$$A_f(t) \propto u_i(t) S_f^{-1}(t) \quad (15)$$

The perturbation of u_i originates from the vorticity shedding and hence the turbulence intensity increases at the sudden area expansion between the main injector nozzle and combustion chamber. This perturbation δu_i takes τ_c to convect to the flame front. Therefore, we define the area perturbation $\frac{\delta A_f(t)}{A_f}$:

$$\frac{\delta A_f(t)}{A_f} = \frac{\delta u_i(t - \tau_c)}{u_i} - \frac{\delta S_f(t)}{S_f} \quad (16)$$

Combing Eq. (12), (13), (16) into Eq. (10),

$$\frac{\delta \dot{Q}}{\dot{Q}} = \frac{\delta u_i(t - \tau_c)}{u_i} - \frac{A_{om} \delta u_{om}(t - \tau_{om}) + A_{im} \delta u_{im}(t - \tau_{im})}{A_i u_i} \quad (17)$$

We define the convective time delay τ_c as the time required for the perturbation, originating at the combustion chamber inlet, convected downstream to the axial flame position, L_f , by the mean chamber velocity, u_i ; τ_{om} as the total time required for a perturbation to travel from the outer main swirler exit to the flame front. This involves first traversing the axial distance L_{om} to the chamber inlet at the mean velocity u_{om} , followed by the convection from the inlet to

the flame front, which takes time τ_c ; τ_{im} as the total time required for a perturbation to travel from the inner main swirler exit to the flame front. Similarly, this involves first traversing the axial distance L_{im} to the chamber inlet at the mean velocity u_{im} , followed by the time τ_c :

$$\tau_c = \frac{L_f}{u_i} \quad (18)$$

$$\tau_{om} = \frac{L_{om}}{u_{om}} + \tau_c \quad (19)$$

$$\tau_{im} = \frac{L_{im}}{u_{im}} + \tau_c \quad (20)$$

Furthermore, a strong vortex roll-up within the jet from the main injector to the combustion chamber acts as a fluid dynamic amplification mechanism, transforming small velocity perturbations downstream of the swirler into significant fluctuations as the flow enters the chamber (Durox et al. 2005). To account for this impact in our model, we introduce an interaction index n in Eq. (17) and obtain our injector-geometry-based flame transfer function, Eq. (21).

$$\frac{\delta \dot{Q}}{\dot{Q}} = n \frac{\delta u_c(t - \tau_c)}{u_i} - n \frac{A_{om} \delta u_{om}(t - \tau_{om}) + A_{im} \delta u_{im}(t - \tau_{im})}{A_i u_i} \quad (21)$$

Bayesian data assimilation

The flame transfer function, Eq. (21), has four uncertain parameters: τ_{om} , τ_{im} , τ_c and n . In the network model, we estimate L_f based on the maximum heat release position of the main flame from the LES results (Reinhardt et al. 2023). The convective velocities u_{om} and u_{im} are the mean bulk velocities within the outer main and inner main swirler passages. However, the propagation speed of the swirler-induced perturbation could have up to 50 % deviation from the mean bulk velocity, observed in experiments (Komarek and Polifke 2010; Palies et al. 2011), large eddy simulations (Müller et al. 2024) and also supported by the linear analysis (Albayrak et al. 2019). Therefore, we assign three coefficients η_{L_f} , $\eta_{u_{om}}$ and $\eta_{u_{im}}$ to correct L_f , u_{om} and u_{im} respectively. For the interaction index n , we use one as the initial guess.

We use the first level of Bayesian inference (Zheng et al. 2024; Juniper and Yoko 2022; MacKay 2003) to find the optimal coefficients to maximise the posterior of Eq. (22), $P(a|D, H)$, where a represents these coefficients, D the 10 microphone measurements, H the flame transfer function, Eq. (17).

$$P(a|D, H) = \frac{P(D|a, H)P(a|H)}{P(D|H)} \quad (22)$$

We assume that the prior $P(a|H)$ and data likelihood $P(D|a, H)$ are Gaussian. We neglect the denominator of Eq. (22) because it is not relevant to the parameters. We then define the cost function, J in Eq. (23), as the negative

log of the numerator, where P_r and P_i indicate the real and imaginary parts of the model predicted pressures; Q_r and Q_i indicate the real and imaginary parts of the measured pressures; C_{P^*} and C_{aa} indicate the prior uncertainties of acoustic pressures and parameters.

$$J = -\log(P(D|a, H)P(a|H)) \\ = \frac{(P_r(a) - Q_r)^T C_{Pr}^{-1} (P_r(a) - Q_r)}{2} \dots \\ + \frac{(P_i(a) - Q_i)^T C_{Pi}^{-1} (P_i(a) - Q_i)}{2} \dots \\ + \frac{(a - a_0)^T C_{aa}^{-1} (a - a_0)}{2} \quad (23)$$

We minimize J with respect to the coefficients, a using gradient-based optimization. The initial coefficients a_0 are defined as 1.

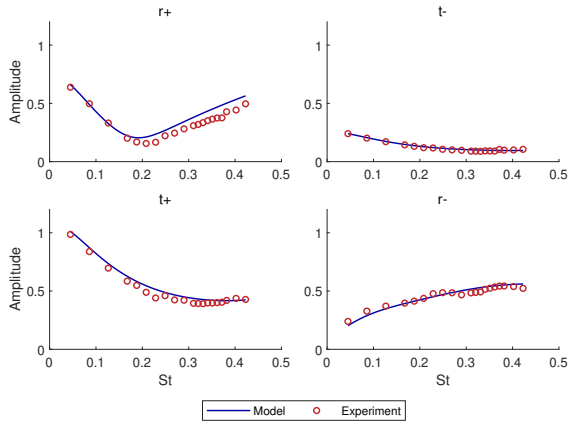
Results and discussion

In this section, we first compare the network model's predictions for both the mean flow and the acoustic field against experimental measurements from the three non-reacting cases (NR1, NR2, NR3). This comparison shows the quantitative accuracy of the network model's predictions and extrapolations across different non-reacting conditions. We then evaluate the network model, which incorporates the injector-geometry-based flame transfer function (FTF) from Eq. (21), by comparing its predictions against experimental data from the main-flame-only reacting case (R1). This evaluation considers the model's performance both before and after data assimilation. The comparison quantifies the sensitivity of the predicted thermoacoustic response to the flame axial position and demonstrates that data assimilation significantly improves the model's accuracy.

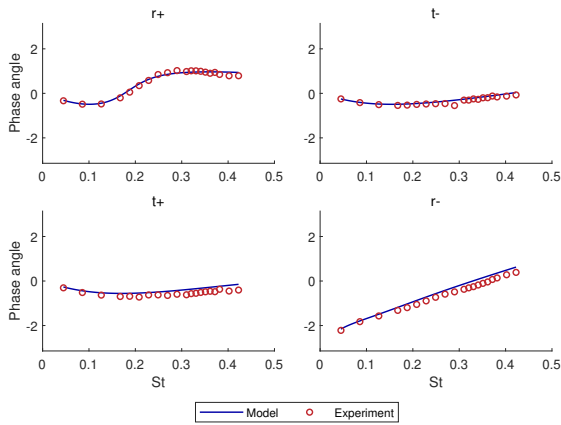
Non-reacting cases Accurate modeling of the non-reacting SCARLET rig serves as the basis for the subsequent thermoacoustic analysis. As presented in Table 2, we first compare measured and predicted values for inlet pressure and the pressure drops across both the metering plate and the injector for non-reacting cases NR1, NR2, and NR3.

Table 2. Comparison of predicted and measured mean flow field parameters in the SCARLET rig across different operating conditions.

Parameter	Case	Experiment	Model
Inlet pressure (MPa)	NR1	1.88	1.88
	NR2	1.53	1.50
	NR3	2.95	2.90
	R1	2.91	2.89
Meter. plate ΔP (%)	NR1	1.27	1.25
	NR2	1.38	1.33
	NR3	1.11	1.09
	R1	1.41	1.33
Injector ΔP (%)	NR1	3.79	3.37
	NR2	4.76	3.60
	NR3	3.81	2.95
	R1	3.79	3.18



(a) Case NR1: Scattering matrix amplitude



(b) Case NR1: Scattering matrix phase angle

Figure 3. Case NR1: Predicted versus measured amplitudes and phase angles of the scattering matrix elements of the test section as a function of Strouhal number (St). The elements are the forward reflection coefficient ($r+$), backward reflection coefficient ($r-$), forward transmission coefficient ($t+$), and backward transmission coefficient ($t-$).

The inlet pressure indicates the overall operating conditions of the SCARLET rig. The pressure drop across the metering plate indicates the mass flow split to the outer annulus, while the injector pressure drop mainly reflects the mechanical energy losses across the injector swirlers (Zheng et al. 2024). The network model predicts these mean flow field parameters with errors below 2 %.

For the acoustic field, there are ten microphones to measure the acoustic response of the test section: five positioned in the upstream duct (labeled microphone 1-5) and five in the downstream duct (labeled microphone 6-10). From these 10 microphone measurements, we obtain the scattering matrix of the test section. Figure 3 compares the predicted and measured amplitudes of the scattering matrix elements of the test section as a function of Strouhal number (St) for case NR1. The elements are the forward reflection coefficient ($r+$), backward reflection coefficient ($r-$), forward transmission coefficient ($t+$), and backward transmission coefficient ($t-$).

As shown in Fig. 3, the network model accurately predicts Case NR1 scattering matrix. In Table 3, we quantify the acoustic network model error by calculating the root mean square error percentage (RMSEP) between predicted and

Table 3. Root Mean Square Error Percentage (RMSEP) of acoustic pressure predictions when forcing from the upstream and downstream ends of the test section for non-reacting cases (NR1, NR2, NR3).

Case	RMSEP Upstream (%)	RMSEP Downstream (%)
NR1	9.7	9.8
NR2	9.7	9.8
NR3	9.9	9.1

measured acoustic pressures at these microphone locations for the non-reacting cases (NR1-NR3). The errors when forcing from the upstream and downstream ends are less than 10 %. Therefore, although we change the operating condition in Table 1, the scattering matrices for the non-reacting cases are quite similar. Figs. 4 and 5 compare the predicted and measured pressure amplitudes and phase angles for case NR1 under the upstream and downstream forcing conditions respectively. Both figures show results as a function of Strouhal number (St) at microphone 3 in the upstream duct and microphone 8 in the downstream duct. From these figures, we find that the network model also predicts the acoustic response at these microphone positions with quantitative accuracy.

Reacting case before and after data assimilation As shown in Table 2, the network model accurately predicts the mean flow field parameters for the reacting case, with associated percent discrepancy below 1 %. Next, we investigate three data assimilation reacting cases: R1 A1, R1 A2 and R1 A3 in Table 4. Case R1 A1 assimilates only the flame position correction coefficient (η_{L_f}). Case R1 A2 assimilates η_{L_f} , the correction coefficients of the convective velocities in the outer main ($\eta_{u_{om}}$) and inner main ($\eta_{u_{im}}$) injectors, while Case R1 A3 assimilated the four investigated coefficients. The assimilation of these parameters does not change the reacting mean flow field. Before data assimilation, all coefficients start from unity and we assign large prior uncertainties ($3\sigma = 1.00$) to the assimilated parameters. After data assimilation, these uncertainties significantly reduce, which means that the model learns a lot of information from the data. In Case R1 A1, the uncertainty for η_{L_f} reduce to 0.01. In Case R1 A2, the uncertainties for η_{L_f} , $\eta_{u_{om}}$ and $\eta_{u_{im}}$ reduce to 0.01, 0.02 and 0.02 respectively. In Case R1 A3, the posterior uncertainties for all parameters are 0.01.

Table 4. Original and assimilated correction coefficients for reacting case R1 under different data assimilation scopes, with 3 standard deviation uncertainties.

Case	Parameter	Before DA ($\pm 3\sigma$)	After DA ($\pm 3\sigma$)
R1 A1	η_{L_f}	1.00 ± 1.00	0.89 ± 0.01
R1 A2	η_{L_f}	1.00 ± 1.00	0.68 ± 0.01
	$\eta_{u_{om}}$	1.00 ± 1.00	0.46 ± 0.02
	$\eta_{u_{im}}$	1.00 ± 1.00	0.43 ± 0.02
R1 A3	η_{L_f}	1.00 ± 1.00	0.65 ± 0.01
	$\eta_{u_{om}}$	1.00 ± 1.00	0.32 ± 0.01
	$\eta_{u_{im}}$	1.00 ± 1.00	0.23 ± 0.01
	n	1.00 ± 1.00	1.30 ± 0.01

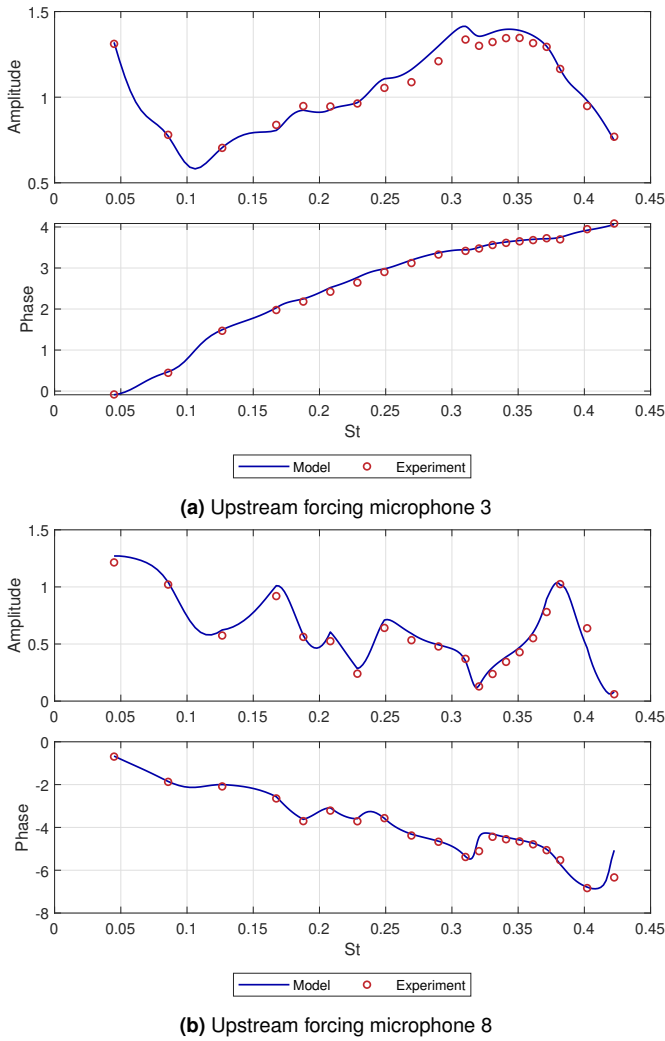


Figure 4. Case NR1: Comparison of predicted and measured pressure amplitudes and phase angles as a function of Strouhal number (St) at microphone 3 and 8 within the SCARLET rig under the upstream forcing condition.

Table 5. Root Mean Square Error Percentage (RMSEP) of acoustic pressure predictions when forcing from the upstream and downstream ends of the test section for reacting case R1 before and after data assimilation.

Case	RMSEP Upstream (%)	RMSEP Downstream (%)
R1	50.3	19.2
R1 A1	40.0	22.1
R1 A2	21.0	22.3
R1 A3	12.3	23.6

For Case R1 A1, the decrease of η_{L_f} to 0.89 corresponds to an adjustment equivalent to 2.8 % of the diameter of the main injector nozzle (see Table 4). This small change in the axial position of the flame reduces the root mean square error percentage (RMSEP) when forcing from the upstream end from 50.3 % to 40.0 % and slightly increases the RMSEP when forcing from the downstream end from 19.2 % to 22.1 %, as shown in Table 5. We can visually investigate this improvement at microphone 3 and 8 when forcing from the upstream and downstream ends in Figs. 7 and 8. Before data assimilation, the network model (case R1) can roughly capture the observed trends at microphone 3 and 8. After

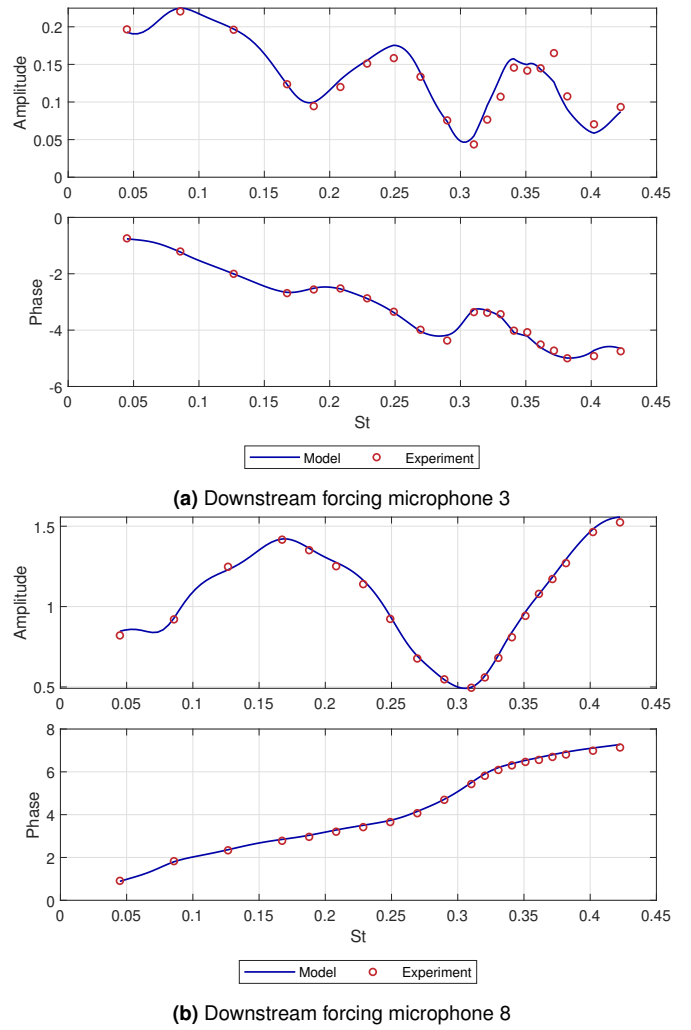
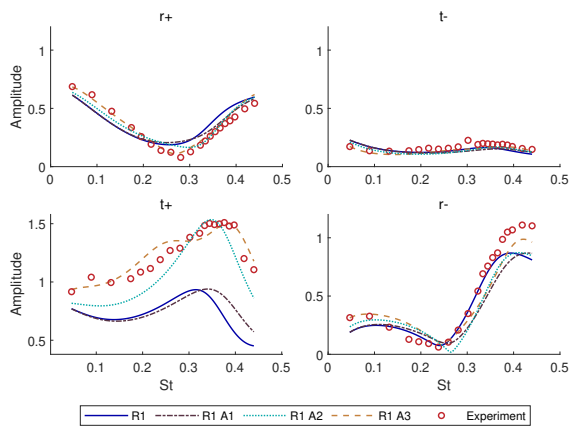


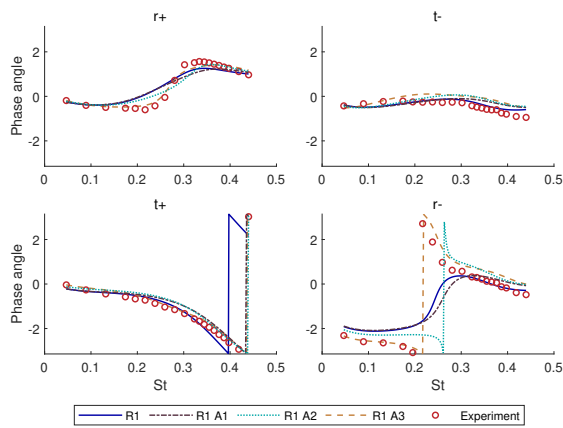
Figure 5. Case NR1: Comparison of predicted and measured pressure amplitudes and phase angles as a function of Strouhal number (St) at microphone 3 and 8 within the SCARLET rig under the downstream forcing condition.

assimilating η_{L_f} (case R1 A1), the model predicts more accurately at microphone 8 when forcing from the upstream end, particularly when $St > 0.25$ (Figs. 7b). However, when forcing from the upstream end, this model underpredicts the acoustic pressure amplitudes within the downstream duct (Figs. 7b).

For Case R1 A2 in Table 4, η_{L_f} decreases to 0.68, $\eta_{u_{om}}$ to 0.46, $\eta_{u_{im}}$ to 0.43. The change of $\eta_{u_{om}}$ indicates the convective speed of the vorticity wave induced by the outer main swirler is 46 % of the bulk mean velocity in its passage. The change of $\eta_{u_{im}}$ indicates the convective speed of the vorticity wave induced by the inner main swirler is 43 % of the bulk mean velocity in its passage. These results disagree with the observations in (Komarek and Polifke 2010; Palies et al. 2011), where the convective velocities are around 50 % faster than the bulk mean velocities. However, the linear analysis in (Albayrak et al. 2019) points out the convective velocity of the vorticity wave could be either faster or slower than the bulk mean velocity. Müller et al. (Müller et al. 2024) find the faster convective speed tends to occur in the weak shear flow and the slower convective speed occurs in the strong shear flow. Within the SCARLET rig, the flows downstream of the inner and outer main swirlers have strong



(a) Scattering matrix amplitude

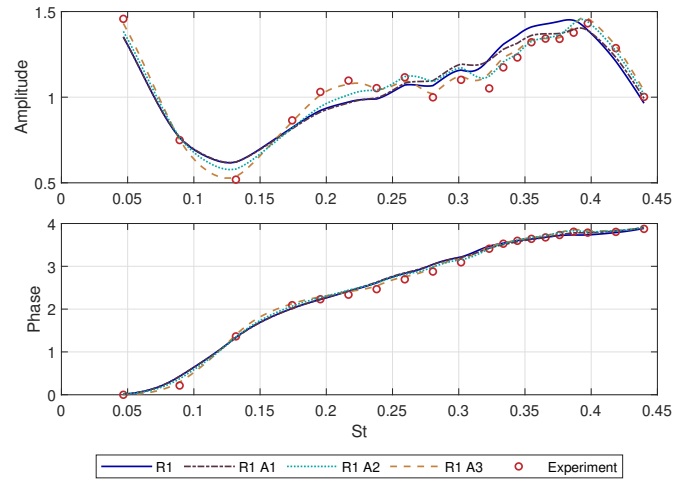


(b) Scattering matrix phase angle

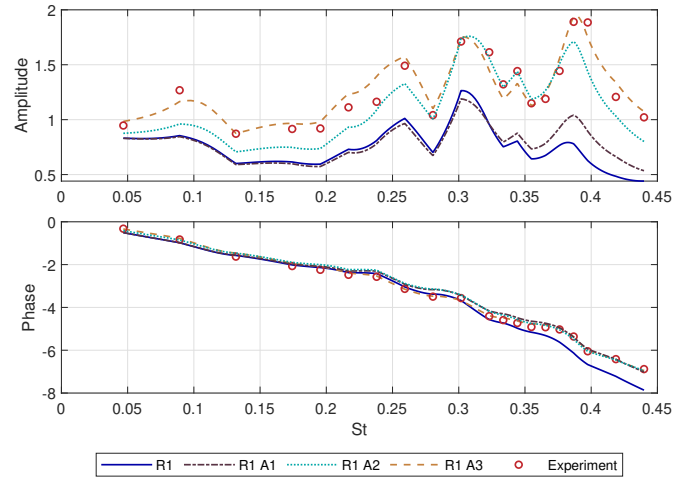
Figure 6. Case R1, R1 A1, R1 A2 and R1 A3: Predicted versus measured amplitudes and phase angles of the scattering matrix elements of the test section as a function of Strouhal number (St). The elements are the forward reflection coefficient ($r+$), backward reflection coefficient ($r-$), forward transmission coefficient ($t+$), and backward transmission coefficient ($t-$).

shear. Furthermore, the merging of these swirling flows at the main injector nozzle generates another strong shear flow region. This could explain why, in Case R1 A2, the vorticity waves convect at speeds slower than the bulk mean velocities within the outer and inner main injectors. The changes of these coefficients reduce the root mean square error percentage (RMSEP) when forcing from the upstream end from 50.3 % to 21.0 % and slightly increase the RMSEP when forcing from the downstream end from 19.2 % to 22.3 %, as shown in Table 5. We can also visually investigate this improvement at different microphone positions when forcing from the upstream and downstream ends in Figs. 7 and 8. The network model for case R1 A2 achieves more accurate predictions than case R1 A1, especially the downstream duct when forcing from the upstream end.

For Case R1 A3 in Table 4, η_{L_f} decreases to 0.65, $\eta_{u_{om}}$ to 0.32, $\eta_{u_{im}}$ to 0.23, and n increases to 1.30. An interaction index of $n = 1.30$ indicates that velocity perturbations originating downstream of the swirler are amplified, resulting in heat release rate fluctuations that are 1.3 times larger in magnitude, which is possibly due to the vortex roll-up within the jet from the main injector to the combustion chamber (Durox et al. 2005). The changes



(a) Upstream forcing microphone 3



(b) Upstream forcing microphone 8

Figure 7. Comparison of predicted and measured pressure amplitudes and phase angles as a function of Strouhal number (St) at microphone 3 and 8 within the SCARLET rig under the upstream forcing condition for case R1, R1 A1, R1 A2 and R1 A3.

of these coefficients reduce the root mean square error percentage (RMSEP) when forcing from the upstream end from 50.3 % to 12.3 % and slightly increase the RMSEP when forcing from the downstream end from 19.2 % to 23.6 %, as shown in Table 5. Fig. 7 shows that Case R1 A3 provides the best fit to the experimental data across all forcing frequencies. In contrast, Fig. 8 reveals that the superiority of this model over the others is not apparent when forcing from the downstream end. The progression from Case R1 to R1 A3 yields a sequential improvement in the prediction of acoustic pressure. Consequently, a corresponding enhancement is observed in the accuracy of the predicted scattering matrix elements in Fig. 6.

For more information Figs. 9 and 10 in the appendix compare the predicted and measured pressure amplitudes and phase angles as a function of Strouhal number (St) at the rest of microphone locations within the SCARLET rig under the upstream and downstream forcing condition for Case NR1. In addition, Figs. 11 and 12 compare similar information for the reacting case before and after data assimilation (Case R1, R1 A1, R1 A2 and R1 A3).

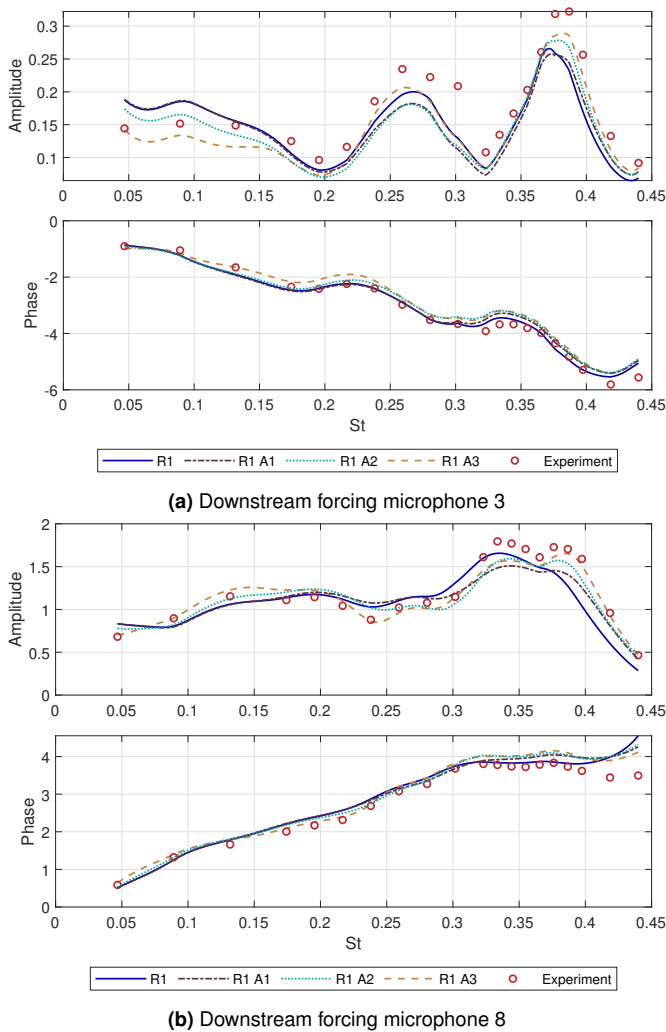


Figure 8. Comparison of predicted and measured pressure amplitudes and phase angles as a function of Strouhal number (St) at microphone 3 and 8 within the SCARLET rig under the downstream forcing condition for case R1, R1 A1, R1 A2 and R1 A3.

Conclusion

This paper shows how to assimilate data from the SCARLET test rig into low order acoustic and flame network models.

For the non-reacting cases, the network models of the complex multi-swirler injector using effective areas derived from experiments demonstrated high fidelity, predicting the mean flow field with less than 2 % discrepancy and the acoustic field with less than 10 % discrepancy across various operating conditions with respect to the measurements. This confirms the model’s capability to capture complex aeroacoustic interactions in a non-reacting environment.

For the reacting case, we develop an injector-geometry-based FTF, but initial predictions reveal significant acoustic discrepancy due to inherent parameter uncertainties. We use Bayesian inference data assimilation to optimize the uncertain parameters within the FTF, improving the model’s predictive accuracy. After assimilation, the LONM predicts the mean flow field with less than 1 % discrepancy and the acoustic field discrepancy reduces to 12.3 % from 50.3 % when forcing from the upstream end, at the cost of a small

increase from 19.2 % to 23.6 % when forcing from the downstream end.

This work highlights the significant potential of integrating low-order models with data assimilation to bridge the gap between computational efficiency and quantitative accuracy. The ability to find optimal model parameters based on experimental data not only improves accuracy but also enhances physical insights into the flame dynamics and thermoacoustic coupling mechanisms.

Future work will involve extending this methodology to various reacting operating conditions within the SCARLET rig. This will allow us to investigate the extrapolability of the FTF to such conditions.

Acknowledgements

Matthew Yoko acknowledges funding from the European Union, under Grant Agreement No 101102004 within the HEAVEN project. Views and opinions expressed are however those of the author(s) only and do not necessarily reflect those of the European Union or Clean Aviation Joint Undertaking. Neither the European Union nor Clean Aviation JU can be held responsible for them.

The experimental work was funded by the European Union, under Grant Agreement No 101102004 within the HEAVEN project. The test rig was funded with financial support by German Federal Ministry for Economic Affairs and Climate Action (BMWK) as part of the AG-Turbo program “COORETEC – AG Turbo 2020” is acknowledged as per resolution of the German Federal Parliament under grant number 03ET2012B.

References

- Aguilar JG, Magri LM and Juniper MP (2017) Adjoint-based sensitivity analysis of low-order thermoacoustic networks using a wave-based approach. *Journal of Computational Physics* 341: 163–181. DOI:10.1016/j.jcp.2017.04.013.
- Albayrak A, Juniper MP and Polifke W (2019) Propagation speed of inertial waves in cylindrical swirling flows. *Journal of Fluid Mechanics* 879: 85–120. DOI:10.1017/jfm.2019.641.
- Cannon SM, Adumitroaie V and Smith CE (2001) 3D LES modeling of combustion dynamics in lean premixed combustors. In: *Proceedings of the ASME Turbo Expo 2001: Power for Land, Sea, and Air*, volume 2. New Orleans, LA, USA: The American Society of Mechanical Engineers (ASME), p. V002T02A056. DOI:10.1115/2001-GT-0375.
- Crocco L (1951) Aspects of combustion stability in liquid propellant rocket motors part i: Fundamentals. low frequency instability with monopropellants. *Journal of the American Rocket Society* 21(6): 163–178. DOI:10.2514/8.4393.
- Culick F (2006) Unsteady motions in combustion chambers for propulsion systems. *NATO RTO-AG-AVT-039, AGARDograph*.
- Dowling AP and Stow SR (2003) Acoustic analysis of gas turbine combustors. *Journal of Propulsion and Power* 19: 751–764.
- Durox D, Schuller T and Candel S (2005) Combustion dynamics of inverted conical flames. *Proceedings of the Combustion Institute* 30(2): 1717–1724. DOI:10.1016/j.proci.2004.08.067.
- Eder AJ, Merk M, Hollweck T, Fischer A, Lahiri C, Silva CF and Polifke W (2024) Model-based inference of flame transfer matrices from acoustic measurements in an aero-engine test rig.

- Journal of Engineering for Gas Turbines and Power* 147(3): 031022. DOI:10.1115/1.4066366.
- Fischer A and Lahiri C (2021) Ranking of aircraft fuel-injectors regarding low frequency thermoacoustics based on an energy balance method. In: *Proceedings of the ASME Turbo Expo 2021: Turbomachinery Technical Conference and Exposition, Turbo Expo*, volume Volume 3B: Combustion, Fuels, and Emissions. p. V03BT04A011. DOI:10.1115/GT2021-59561.
- Han X and Morgans AS (2015) Simulation of the flame describing function of a turbulent premixed flame using an open-source les solver. *Combustion and Flame* 162(5): 1778–1792. DOI: 10.1016/j.combustflame.2014.11.039.
- Hubbard S and Dowling A (2001) Acoustic resonances of an industrial gas turbine combustion system. *Journal of Engineering for Gas Turbines and Power-transactions of The ASME - J ENG GAS TURB POWER-T ASME* 123. DOI: 10.1115/1.1370975.
- Juniper MP and Sujith RI (2018) Sensitivity and nonlinearity in Thermoacoustics. *Annual Review of Fluid Mechanics* 50: 661–689. DOI:10.1146/annurev-fluid-122316-045125.
- Juniper MP and Yoko M (2022) Generating a physics-based quantitatively-accurate model of an electrically-heated Rijke tube with Bayesian inference. *Journal of Sound and Vibration* 535: 117096. DOI:10.1016/j.jsv.2022.117096.
- Komarek T and Polifke W (2010) Impact of swirl fluctuations on the flame response of a perfectly premixed swirl burner. *Journal of Engineering for Gas Turbines and Power* 132(6): 061503. DOI:10.1115/1.4000127.
- MacKay DJC (2003) *Information Theory, Inference, and Learning Algorithms*. Copyright Cambridge University Press.
- Müller J, von Saldern J, Kaiser T and Oberleithner K (2024) Linear amplification of inertial-wave-driven swirl fluctuations in turbulent swirling pipe flows: a resolvent analysis approach. *Journal of Fluid Mechanics* 1000: A91. DOI:10.1017/jfm.2024.679.
- Palies P, Durox D, Schuller T and Candel S (2011) Experimental study on the effect of swirler geometry and swirl number on flame describing functions. *Combustion Science and Technology* 183: 704–717. DOI:10.1080/00102202.2010.538103.
- Poinsot T (2017) Prediction and control of combustion instabilities in real engines. *Proceedings of the Combustion Institute* 36(1): 1–28. DOI:10.1016/j.proci.2016.05.007.
- Polifke W and Lawn C (2007) On the low-frequency limit of flame transfer functions. *Combustion and Flame* 151(3): 437–451. DOI:10.1016/j.combustflame.2007.07.005.
- Reinhardt H, Alanyalıoğlu ÇO, Fischer A, Lahiri C, Nicolai H and Hasse C (2023) Simulation of the thermoacoustic response of an aero-engine gas turbine fuel injector using a hybrid cfd-caa method. *Journal of Engineering for Gas Turbines and Power* 145: 1–11. DOI:10.1115/1.4063335.
- Schuermans B, Bellucci V, Guethe F, Meili F, Flohr P and Paschereit CO (2004) A detailed analysis of thermoacoustic interaction mechanisms in a turbulent premixed flame. In: *Proceedings of the ASME Turbo Expo 2004: Power for Land, Sea, and Air, Turbo Expo*, volume 1. ASME, pp. 539–551. DOI:10.1115/GT2004-53831.
- Yoko M and Juniper MP (2024) Adjoint-accelerated bayesian inference applied to the thermoacoustic behaviour of a ducted conical flame. *Journal of Fluid Mechanics* 985: A38. DOI: 10.1017/jfm.2024.276.
- Zheng J, Fischer A, Lahiri C, Yoko M and Juniper MP (2024) Bayesian data assimilation in cold flow experiments on an industrial thermoacoustic rig. *Journal of Engineering for Gas Turbines and Power* 147(5): 051008. DOI:10.1115/1.4066611.
- Çetin Ozan Alanyalıoğlu, Reinhardt H, Fischer A, Lahiri C, Nicolai H and Hasse C (2024) Comparison of acoustic, optical, and heat release rate based flame transfer functions for a lean-burn injector under engine-like conditions. *International Journal of Spray and Combustion Dynamics* 16(3): 153–173. DOI: 10.1177/17568277241270403.

Appendix

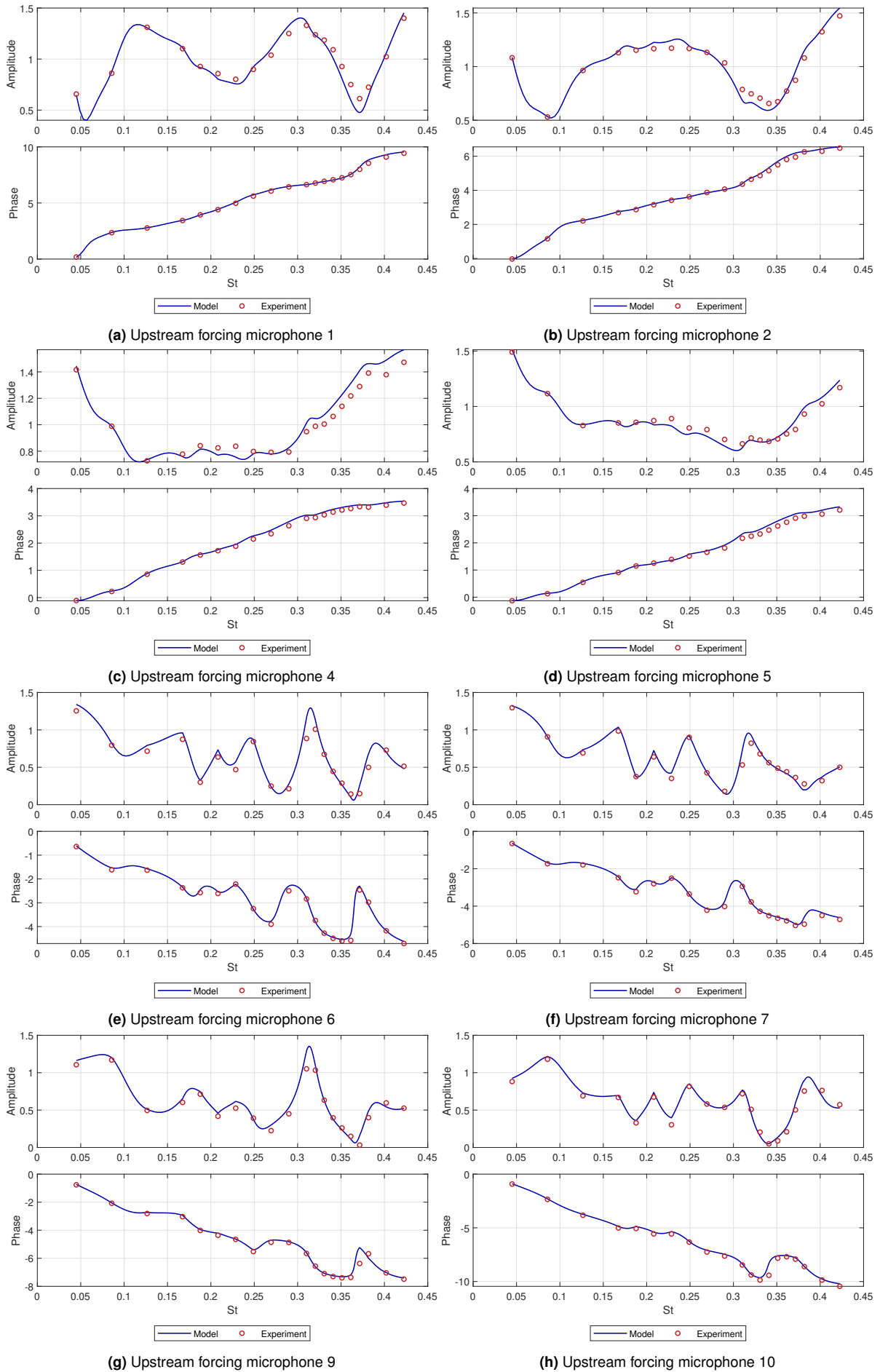


Figure 9. Case NR1: Comparison of predicted and measured pressure amplitudes and phase angles as a function of Strouhal number (St) at different microphone locations within the SCARLET rig under the upstream forcing condition.

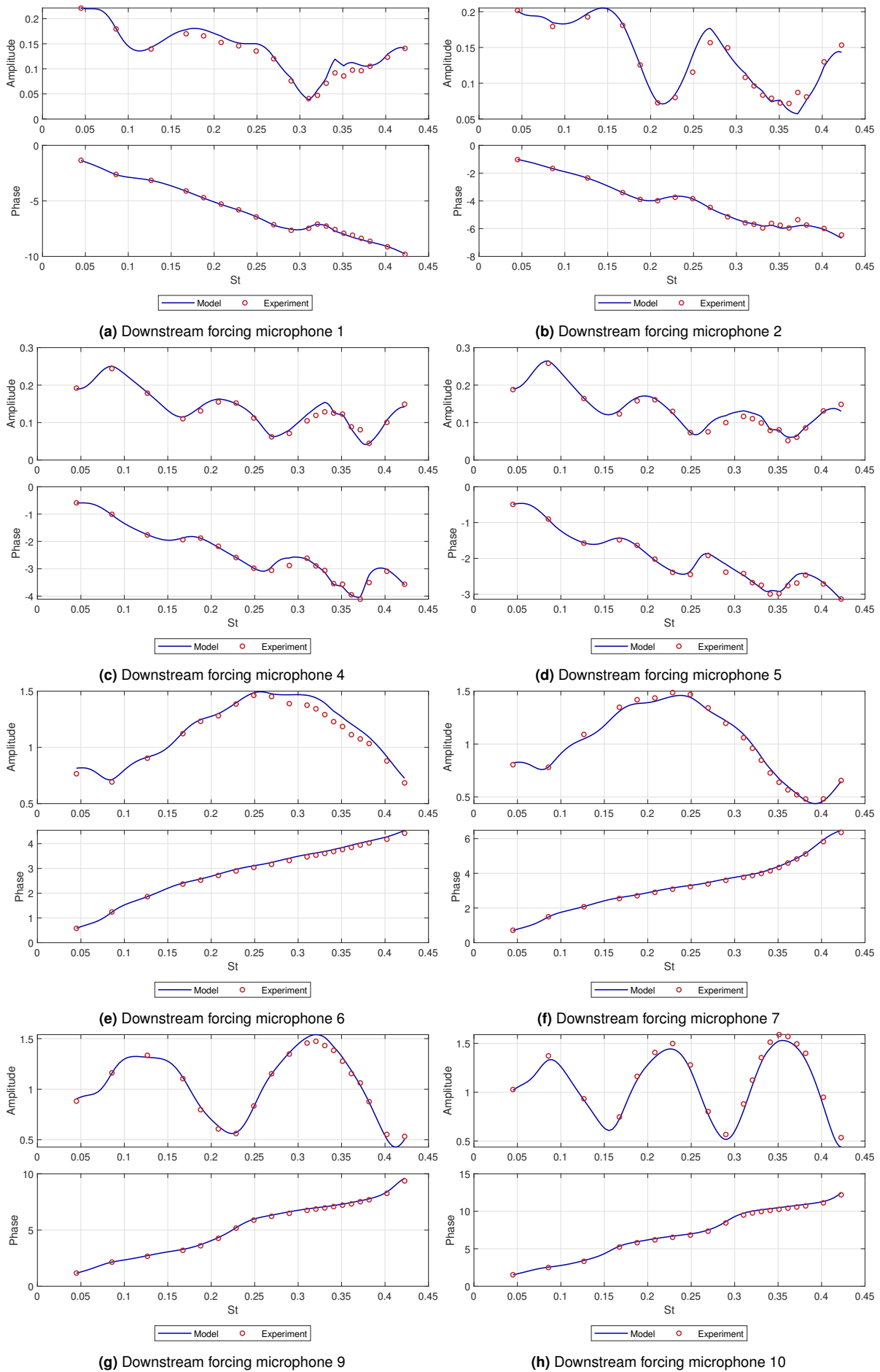


Figure 10. Case NR1: Comparison of predicted and measured pressure amplitudes and phase angles as a function of Strouhal number (St) at different microphone locations within the SCARLET rig under the downstream forcing condition.

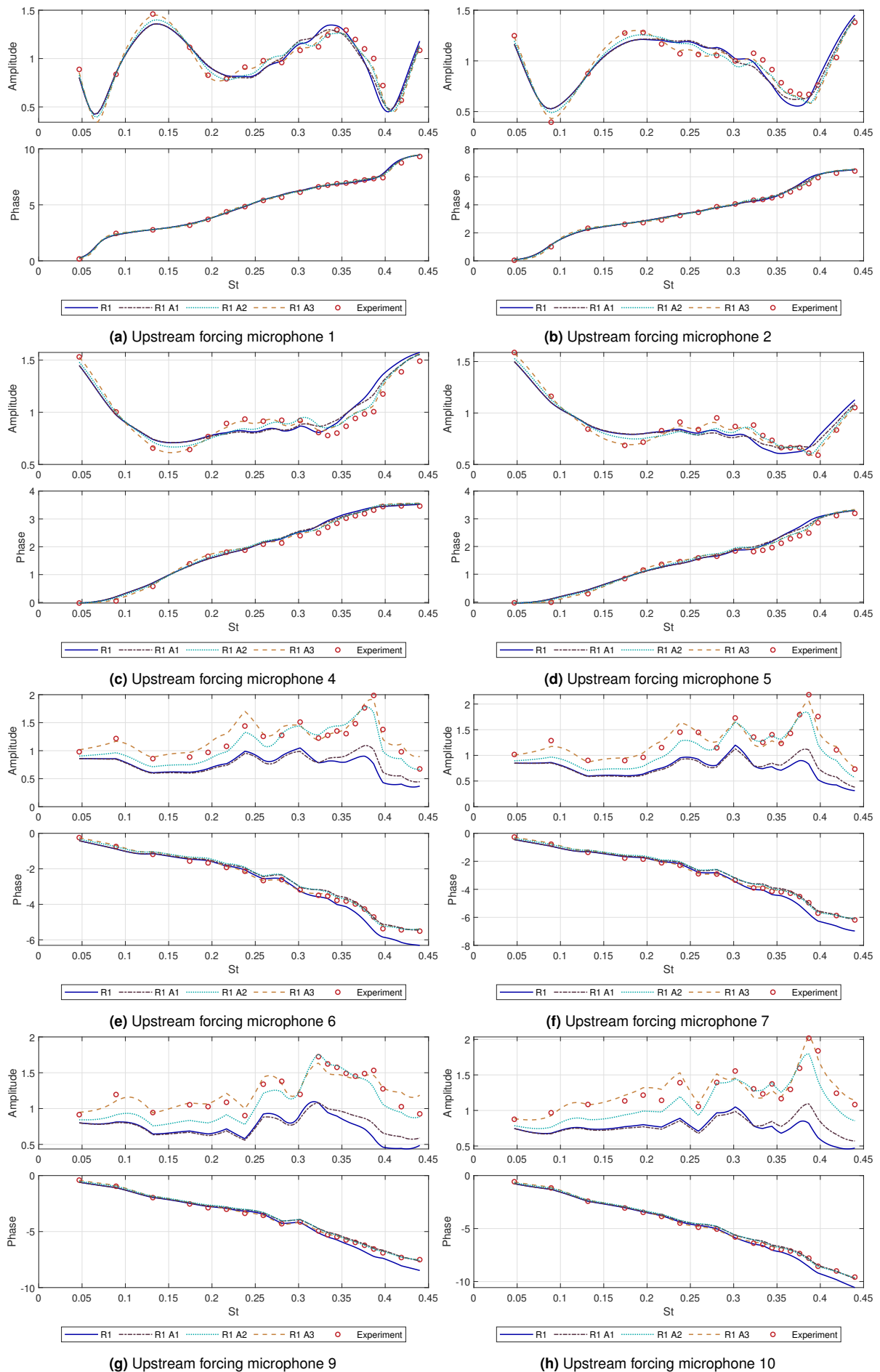


Figure 11. Comparison of predicted and measured pressure amplitudes and phase angles as a function of Strouhal number (St) at different microphone locations within the SCARLET rig under the upstream forcing condition for case R1, R1 A1, R1 A2 and R1 A3.

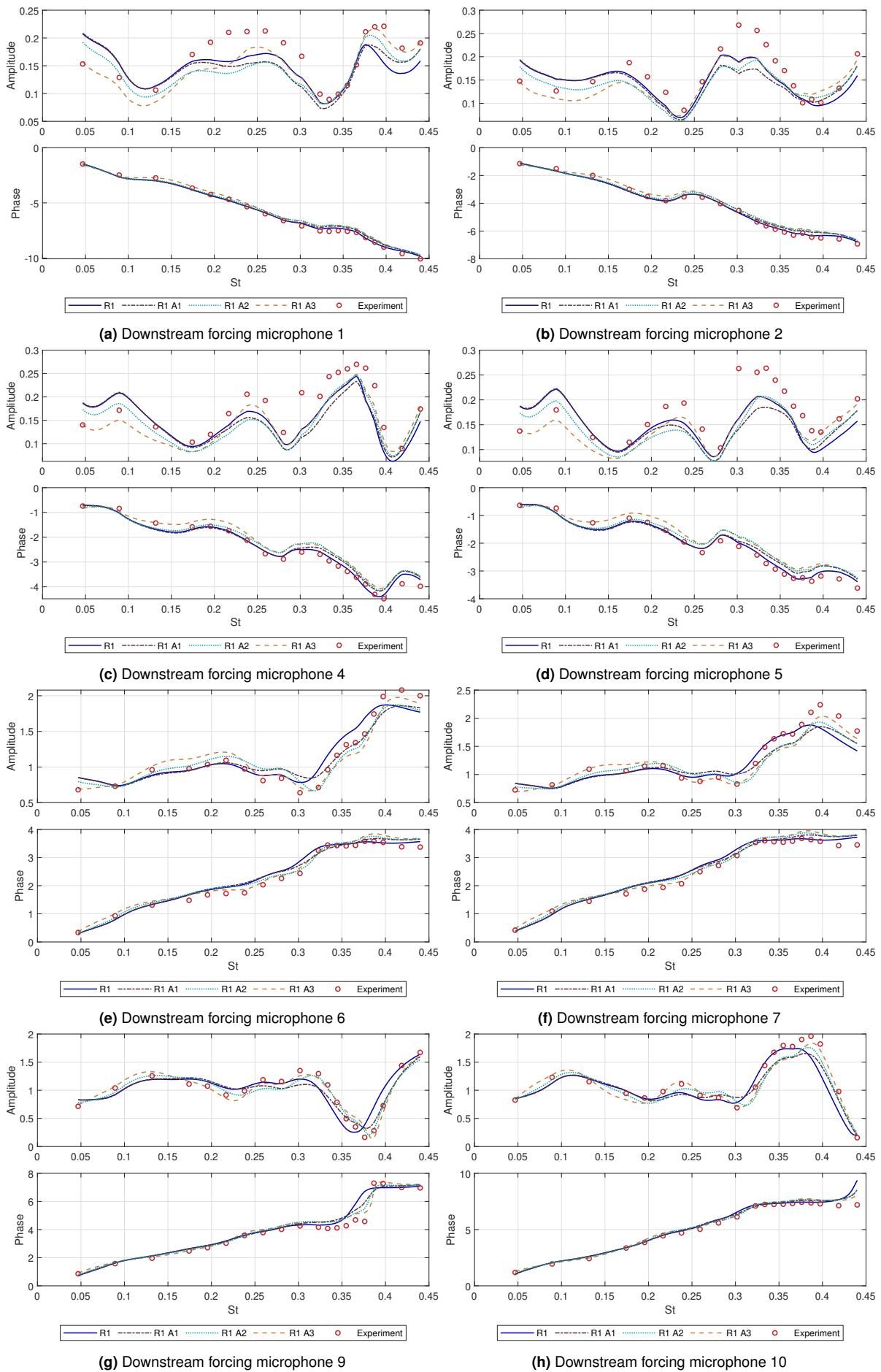


Figure 12. Comparison of predicted and measured pressure amplitudes and phase angles as a function of Strouhal number (St) at different microphone locations within the SCARLET rig under the downstream forcing condition for case R1, R1 A1, R1 A2 and R1 A3.